

Investigating the Effects of Tip Modification on High-Frequency Noise Emission of CART II Wind Turbine using a Hybrid Computational Aeroacoustic Approach

S. H. Delbari¹, A. Nejat^{2†} and A. Hajinezhad¹

¹ *University of Tehran- Faculty of New Sciences and Technologies 1, Tehran, Tehran, Iran*

² *University of Tehran- School of Mechanical Engineering, Tehran, Tehran. Iran*

† *Corresponding Author Email: nejat@ut.ac.ir*

(Received October 18, 2021; accepted March 9, 2022)

ABSTRACT

This study carries out computational aeroacoustic calculations around the tip region of the CART II wind turbine blade. Additionally, two modified tip designs, namely; tip O and tip R, are further investigated to determine how the geometry of the tip region affects the noise emission characteristics of the wind turbine. The study focuses on the tip vortex noise mechanism using hybrid computational aeroacoustic to tackle the issue of the enormous computational power required for direct noise simulation. Improved Delayed Detached Eddy Simulation (IDDES) technique is used to calculate the instantaneous turbulent flow field near the sound source region, and the noise prediction in far-field is performed using the Ffowcs Williams and Hawking's (FW-H) acoustic analogy. The method visualizes the flow field near the blades' tip, assisting researchers to have an accurate understanding of aerodynamically induced noise mechanisms in that highly complex flow region, thus being able to modify tip design in a way that contributes to lower overall noise emission. The results for the outboard section of the CART II wind turbine's blade are validated with experimental data. Broadband noise sources such as turbulent-boundary-layer trailing-edge (TBL-TE) noise and the tip vortex noise mechanisms are investigated for the base case as well as tip O and tip R. The results show that the overall sound pressure level (OASPL) and the generated torque of tip R and tip O, are 2.0 %, 5.0 % and 0.8 %, 2.2 % lower than the base case, respectively.

Keywords: Horizontal axis wind turbine; Aerodynamic noise; Turbulence; Ffowcs Williams and Hawkings acoustic analogy; Improved delayed detached eddy simulation.

1. INTRODUCTION

The growing trend of global energy demand accompanied by the harmful effects of fossil fuels overexploitation, namely, global warming and climate change, leads to a gradual shift from conventional energy sources to reliable and clean renewable energies (Mostafaeipour 2013).

Among renewable sources, harvesting energy from wind is most promising, and its usage has vastly increased over the recent decades (Dai *et al.* 2015). Horizontal axis wind turbines (HAWTs) as wind energy converters are medium to large scale rotating machinery, which their technologies have been developed substantially during the last decades, leading to significant performance improvement.

Despite considerable progress in the aerodynamic improvement of the HAWTs, wind energy still has certain drawbacks that hinder wind turbines' extensive applications. One of the wind energy usage

challenges is acoustic pollution caused by operating in unsteady flow conditions and dynamic loading exerted on wind turbine blades, which leads to their societal rejection in developed residential areas (Cai *et al.* 2016).

Aeroacoustic emission from wind turbines causes inconveniences for inhabitants in neighborhoods with low ambient noise levels (Jianu *et al.* 2012). Moreover, the average size of wind turbines, especially HAWTs, is continuously growing, causing higher noise emissions. Therefore, investigating and modeling the wind turbine noise must be considered indispensable during the design process (Kaviani and Nejat 2017). Proper geometrical design, including optimizing airfoil sections and tip region would improve both aerodynamic and aeroacoustic characteristics of a wind turbine or, at least, enhance the latter without notably affecting the former (Göçmen and Özerdem 2012).

The sound emitted from a wind turbine can be categorized into mechanical noise and aerodynamic noise. Mechanical noise emanates from the components in the hub and nacelle of the turbine, such as the gearbox, generator, and cooling fans, and is caused by structural vibration. Due to the advanced fabrication processes involved in wind turbine's mechanical equipment production, this source of noise has significantly reduced over the past few years. Aerodynamic noise, however, is radiated from the blades and is mainly associated with the flow turbulence interaction with the blade surface (Wagner *et al.* 1996). Turbulence appears either as the inflow's free turbulence or flow instabilities inside the boundary layer, encompassing the blade's surface. Generally, aerodynamic noise sources can be divided into three main components, namely, low-frequency noise, inflow turbulence noise, and airfoil self-noise (Oerlemans 2009). Since the mechanical noise, unlike aerodynamic noise, does not scale up proportionally to the wind turbine size, the aerodynamic noise dominates as the size of the turbine increases. Therefore, forthcoming studies should focus on developing a better understanding of aerodynamic noise mechanisms to devise the methods contributing to overall noise emission reduction in wind turbines.

Wind turbine's aeroacoustics covers both experimental and computational studies aiming to predict aerodynamic noise perceived by a given observer in the far-field region and detect the aerodynamic noise sources distribution on the blade surface. Although numerous researchers have extensively studied the aeroacoustic characteristics of vertical axis wind turbines (VAWTs) (Ghasemian and Nejat 2015a; Hamid 2019; Mohamed 2014, 2016), the large body of literature deals with HAWTs noise emission studies.

Arakawa *et al.* (2005) performed a finite-volume compressible large eddy simulation to directly resolve both aeroacoustic and aerodynamic fields in the immediate vicinity of a blade of WINDMELL III wind turbine. This study aimed to measure and visualize the tip vortex noise mechanism around the blade's tip region. To directly resolve the near-field acoustic pressure perturbations, a highly dense grid with 320 million elements, which demanded enormous computational power, was developed around the blade. The computations were carried out using the Earth Simulator, the most powerful supercomputer of that time. The results showed that modifying the tip region significantly reduces the Sound Pressure Level (SPL) at the high-frequencies range.

Cho *et al.* (2010) investigated the acoustic characteristics of a scaled model of the NREL Phase VI wind turbine. Using a microphone array, they detected the positions of noise sources on the blade's surface. The result showed that the main noise source at the high-frequencies range shifts toward the outer part of the blade near the tip. Furthermore, in the stall condition, the noise level for frequencies below 2 kHz increases significantly, showing the tonal characteristic of the separation/stall noise mechanism.

Mo and Lee (2011) numerically predicted aeroacoustics of the NREL Phase VI wind turbine, with a focus on the low-frequency noise using incompressible large eddy simulation and FW-H acoustic analogy. The results showed continuous growth of SPL at the frequency range of 300 Hz to 500 Hz as wind speed increases. The authors suggested the tip-vortex-trailing-edge interaction, caused by local crossflow along the trailing edge and in the vicinity of the blade's tip emanates intense aerodynamic noise, which subsequently leads to a higher level of sound pressure at the mentioned frequency range. Additionally, the calculated result of the SPL was compared with semi-empirical models of previous researchers and agreed well with the result reported by Hagg of the other two models.

Tadamasa and Zangeneh (2011) performed aeroacoustic simulations of the NREL Phase VI blade. The resolved unsteady flow field using the SST $k-\omega$ model was fed into the FW-H analogy as a source input to predict the noise at a given observer's location. The simulation result related to the case with a rotor speed of 72 rpm, corresponding to a tip Mach number of 0.12, indicated that quadrupole sources are not as prominent as the loading sources in the total noise. They also found that the intensity of the loading noise has a direct relationship with wind speed.

Lee (2014) conducted numerical, and experimental analyses to predict aerodynamic noise produced by blades of a 10-kW wind turbine. This study shows that the trailing edge bluntness noise is an important aerodynamic noise source for small-scale wind turbines unless the blades have a sharp trailing edge.

Ghasemian and Nejat (2015b) predicted the far-field aerodynamic noise of the NREL Phase VI blade. The aeroacoustic simulation was conducted using FW-H acoustic analogy. The improved delayed detached eddy simulation (IDDES) method was used to resolve the instantaneous flow field in the vicinity of the acoustic source region, and the resulting time-dependent surface pressure fluctuations were recorded as the acoustic source field data. The effect of the inflow wind speed and the receiver's location was investigated and was found that the noise amplitude is directly correlated to the former while being inversely correlated to the latter.

Wasala *et al.* (2015) conducted a large eddy simulation of an outboard section of CART II wind turbine to assess its aeroacoustic characteristics. The result was in good agreement with the experimental data. It was revealed that at high-intensity free turbulence conditions, the main noise source shifts from the suction side's trailing edge to its leading edge. Calculating the spatial distribution of the acoustic field revealed dipole directivity of the high-frequencies noise and the omnidirectional nature of the low-frequencies one.

Kaviani and Nejat (2017) conducted aeroacoustic prediction of the WP_Baseline 1.5 MW HAWT using both CFD and FW-H acoustic analogy as well as the Improved Blade Element Momentum (IBEM) and the semi-empirical methods for noise prediction developed by Brooks, Pope, and Marcolini (BPM).

Two numerical methods were validated against the experimental data, and it was observed that at frequencies above 1 kHz, calculated SPL using IDDES and FW-H method is more consistent with the experimental data.

Previous studies of HAWT noise used either URANS or LES approach, which the former lacks accuracy, and is poorly suited for predicting separated flow and the latter is computationally expensive. Additionally, a large body of literature investigates the aeroacoustics of wind turbines generally, and only a few studies have recently considered specific airfoil self-noise mechanisms such as tip vortex noise, (Ebrahimi and Mardani 2018; Maizi *et al.* 2018; Solís-Gallego *et al.* 2018).

Although Arakawa conducted a thorough study on the tip vortex noise mechanism, the method he used is prohibitively expensive to be implemented for industrial applications.

This study focuses on one of the most important yet fairly unknown aerodynamic noise mechanisms, i.e., the tip vortex noise, using the hybrid computational aeroacoustic to acquire a better understanding of this mechanism and to tackle the issue of the enormous computational power required for direct noise simulation. The visualization of the flow field near the blade's tip region assists researchers to have an accurate understanding of aerodynamically induced noise mechanisms in that highly complex flow region, thus being able to propose various designs to lower overall noise emission. Accordingly, the main objective of the paper is to present the practice of the hybrid method for reliable investigation of the tip vortex noise while keeping it affordable within the current computational cost limit.

In this paper, Improved Delayed Detached Eddy Simulation (IDDES) was applied to capture the unsteady aerodynamic field around the outboard section of the CART II blade and two modified tip profiles, namely, type O and R. The study is a three-dimensional time-accurate CFD simulation for aerodynamic noise prediction of the flow near the tip region of the mentioned geometries. IDDES technique is used to obtain the instantaneous surface pressure perturbations, which are then fed as acoustic source data to the FW-H acoustic analogy to perform noise calculations. As stated above, this study focuses on the tip vortex and tip vortex- trailing edge interaction noises that are the dominant noise sources for large-scale wind turbines with high tip Mach numbers. Calculations were performed for a given inflow condition of $U_\infty = 10.8 \text{ m s}^{-1}$ and turbulent intensity of 10.3%. The result of the base case was compared with the experimental data (Moriarty 2004), then the contours of vorticity and graphs of SPL for all cases were investigated to obtain a better understanding of the flow field near the tip region and to study the effect of tip vortices in the OASPL.

In the next section, a brief survey of computational aeroacoustic is presented. Two main approaches are discussed, and different numerical methods included in each approach are described. In section 3 mathematical expressions of aeroacoustic and

aerodynamic fields as well as sound propagation phenomena involved in the numerical modeling are thoroughly discussed. The geometry of the blade, enclosed in a computational domain with its corresponding boundary and temporal conditions and the applied meshing technique, is introduced in section 4. This section also includes discretizational methods used to solve the flow field around the wind turbine blade. The validation of the base case and aeroacoustic results of all three cases are presented in section 5. Finally, the paper concludes in section 6.

2. COMPUTATIONAL AEROACOUSTICS

There are various conceptual approaches to the prediction of aerodynamic noise mechanisms. Figure 1 illustrates a schematic overview of computational aeroacoustics methods. Based on Fig. 1, two main approaches are distinguished.

1. Direct methods that resolve the acoustic field immediately without any modeling so the sound can be computed directly. A DNS is considered the most exact solution. The fully coupled set of Navier-Stokes equations is solved, thus no additional modeling is required in this method. The direct method has disadvantages such as; the high requirement of computational power (cost of DNS is proportioned to Re^3) and the inherent multi-scale problem in CAA. The latter originates from the different scales of acoustic perturbations compared to the aerodynamic ones and the difference between the speed of sound propagation and fluid propagation, especially in the low-Mach flow regime.

2. Hybrid methods decouple the sound generation and acoustic sound propagation phenomenon. The acoustic sources are identified using one of the following approaches:

(a) Classical CFD methods such as; incompressible and compressible LES/DES can resolve the noise sources almost as accurately as the DNS method.

(b) CFD method in which the sources are statistically reconstructed. In this method, the mean turbulent quantities are provided by Reynolds averaged Navier-Stokes equations (RANS) models. Recently, novel statistical methods have been developed to synthesize a turbulent field based on the resolved time-averaged RANS flow field. This information is subsequently used as the source terms in a separate acoustic prediction model. The accuracy of this method highly depends on the correctness and soundness of the empiric coefficients and the validation data used to regulate them.

(c) LES method coupled with the acoustic perturbation equations (APE) (Ewert and Schröder 2004). LES is used to solve the unsteady flow problem, i.e., capturing the turbulent structures in the near-field aerodynamic, and subsequently apply an acoustic analogy based on linear acoustic perturbation equations (APE) to determine the sound propagated into the far-field. The APE acoustic analogy considers mean-flow convection and

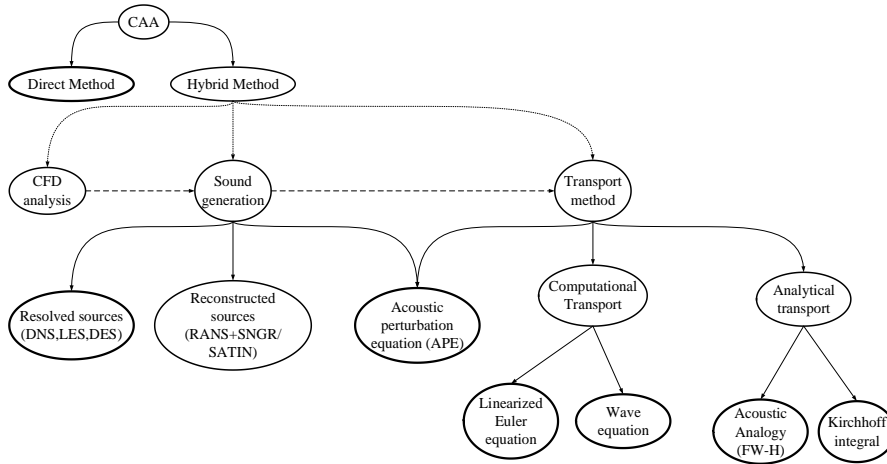


Fig. 1. Computational aeroacoustics approaches.

refraction effects of an inhomogeneous mean flow. Hence, the computational domain of the LES must encompass only the region in the immediate vicinity of the acoustic source region. This approach requires a relatively high computational cost and which is its only disadvantage.

3. GOVERNING EQUATIONS

3.1 IDDES Formulation

The three-dimensional unsteady incompressible form of Navier-Stokes equations has been solved by the Improved Delayed Detached Eddy Simulation technique. IDDES formulation is based on Menter's shear stress transport (SST $k-\omega$) two-equation turbulence model which length scale of the dissipation rate term in the turbulent kinetic energy (TKE) transport equation is appropriately modified (Menter 1994).

$$\frac{\partial}{\partial t}(\rho k) + \frac{\partial}{\partial x_j}(\rho u_j k) = \frac{\partial}{\partial x_j} \left[\left(\mu + \frac{\mu_t}{\sigma_k} \right) \frac{\partial k}{\partial x_j} \right] + \tau_{ij} S_{ij} - \frac{\rho k^{\frac{3}{2}}}{L_{IDDES}} \quad (1)$$

Where $\rho, k, u_j, \mu, \mu_t, \tau_{ij}$ and S_{ij} stand for the density, turbulent kinetic energy, velocity, molecular and turbulent viscosity, tensor of stress and mean strain rate, respectively.

IDDES length scale is developed from the combination of both RANS and LES length scales and is presented as the following (Xiao *et al.* 2015):

$$L_{IDDES} = \check{f}_d(1 + f_e)L_{RANS} + (1 + \check{f}_d)L_{LES} \quad (2)$$

Where the RANS and the LES length scales are defined as the following:

$$L_{RANS} = \frac{\sqrt{k}}{\beta^* \omega} L_{LES} = C_{DES} \Delta \quad (3)$$

The grid scale Δ is defined as, $\min\{\max\{c_w \Delta_{max}, c_w d, \Delta_{min}\}\}$ where c_w is an empirical constant. d is the distance to the nearest wall, Δ_{max} is $\min\{\Delta_x, \Delta_y, \Delta_z\}$. The function \check{f}_d is

defined as $\max\{(1 - f_{dt}), f_B\}$ which is determined by both the geometry part f_B and the flow part $(1 - f_{dt})$.

Further detail about the proposed formulation can be found in Shur *et al.* (2008).

3.2 Aeroacoustics Analogy

In this paper, the most general form of Lighthill's acoustic analogy, the FW-H equation, is exploited for modeling noise propagation. The Ffowcs Williams and Hawkings equation is inherently an inhomogeneous wave equation which can be obtained by rearranging the continuity equation and Navier-Stokes equations (Williams and Hawkings 1969). It is the developed form of Lighthill's acoustic analogy by including the effect of the moving solid body. The FW-H equation can be written as the following:

$$\frac{1}{c_0^2} \frac{\partial^2 p'}{\partial t^2} - \frac{\partial^2 p'}{\partial x_i^2} = \frac{\partial^2}{\partial x_i \partial x_j} T_{ij} H(f) - \frac{\partial}{\partial x_i} [P_{ij} n_j + \rho u_i (u_n - v_n)] \delta(f) + \frac{\partial}{\partial t} [\rho_0 v_n + \rho (u_n - v_n)] \delta(f) \quad (4)$$

Where u_n and u_i are the fluid velocity in the direction normal to the integration surface and in the x_i direction, respectively. v_n is the normal velocity of the integration surface, $H(f)$ is Heaviside function and $\delta(f)$ is Dirac delta function. Subscript 0 refers to the unagitated properties of a medium while the difference between the real and the undisturbed properties is defined by the primed variables (e. g. $p' = p - p_0$).

$f = 0$ Represents a mathematical surface encircling the exterior flow problem ($f > 0$) in an unbounded space. It can be either a rigid body (impermeable) or an off-surface boundary enclosing the rigid body (permeable). n_i is the unit normal vector pointing toward the exterior region ($f > 0$), C_0 is the far-field sound speed and T_{ij} is the Lighthill stress tensor, given by the following equation:

$$T_{ij} = \rho u_i u_j + P_{ij} - c_0^2 (\rho - \rho_0) \delta_{ij} \quad (5)$$

The right-hand side of the FW-H equation represents different sound generation mechanisms. The first

term includes the Lighthill stress tensor and shows that the time-dependent stresses such as momentum, viscosity, and turbulence generate sound. P_{ij} is the compressive stress tensor, including the surface viscous and aerodynamic pressure stress. The compressive stress tensor for a Stokisian fluid is defined as the following:

$$P_{ij} = p\delta_{ij} - \mu \left[\frac{\partial u_i}{\partial x_j} + \frac{\partial u_j}{\partial x_i} - \frac{2}{3} \frac{\partial u_k}{\partial x_k} \delta_{ij} \right] \quad (6)$$

The second term, involving the external forces, is called dipole or loading noise. Finally, the last source term includes the mass flow rate is monopole or thickness noise.

The FW-H equation can be integrated analytically under the assumption of the unbounded flow and the absence of obstructions between the emission source and the receivers. The complete solution consists of surface and volume integrals. Since thickness and loading terms are surface distribution sources, the contributions from monopole, dipole, and partially quadrupole sources are represented by the surface integrals, whereas quadrupoles are volumetric sources in the region outside the source surface, thus are represented by volumetric integrals. The contribution of the volume integrals becomes negligible when the flow is low subsonic, and the source surface encompasses the source region can be omitted. Thus, acoustic pressure p' mentioned in the FW-H is presented as follows:

$$p'(\vec{x}, t) = p'_T(\vec{x}, t) + p'_L(\vec{x}, t) \quad (7)$$

In Eq. (7) t is the observer time, \vec{x} is the receiver position, the subscripts T and L refer to the thickness (monopole) and loading (dipole) components, respectively, and are as follows (Brentner 1987):

$$4\pi p'_T(\vec{x}, t) = \int \left[\frac{\rho_0(U_n + Un)}{r(1-M_r)^2} \right]_{f=0} ds + \int \left[\frac{\rho_0 U_n (rM_r + c_0(M_r - M^2))}{r^2(1-M_r)^3} \right]_{f=0} ds \quad (8)$$

$$4\pi p'_L(\vec{x}, t) = \frac{1}{c_0} \int \left[\frac{L_r}{r(1-M_r)^2} \right]_{f=0} ds + \int \left[\frac{L_r - L_M}{r(1-M_r)^2} \right]_{f=0} ds + \int \left[\frac{L_r (rM_r + c_0(M_r - M^2))}{r^2(1-M_r)^3} \right]_{f=0} ds \quad (9)$$

Where;

$$U_i = v_i + \frac{\rho}{\rho_0}(u_i - v_i)$$

$$L_i = P_{ij}\hat{n}_j + \rho u_i(u_n - v_n) \quad (10)$$

The various subscripted quantities appeared in Eqs. (8) and (9) are the inner products of a vector and a unit vector. They are indexed in this way for brevity. For instance, $L_r = \vec{L} \cdot \hat{r} = L_i r_i$ and $U_n = \vec{U} \cdot \vec{n} = U_i n_i$ where \hat{r} and \vec{n} indicate the unit vectors in the radiation and wall-normal directions, respectively. The Mach number vector M_i is the local surface velocity vector divided by the free stream sound

speed. The dot over a variable denotes the source-time differentiation of that variable. The square brackets in the above equations denote that the integrands are evaluated with respect to the retarded time τ , defines as follows:

$$\tau = t - \frac{r}{c_0} \quad (11)$$

Where t , r , and c_0 are receiver time, the distance to the receiver and the sound speed, respectively.

4. PROBLEM DESCRIPTION

The Control Advanced Research Turbine II (CART II) is a two-blade Westinghouse 600 kW horizontal axis wind turbine with a 42 m rotor diameter and 36.6 m hub height. The blade consists of modified LS (1)-0417 airfoil sections with variable chord lengths in the span-wise direction. Further details about the blade geometry can be found in Stol (2004). The rated output of CART II is 660 kW at 41.7 RPM resulting in the tip speed ratio and tip velocity of 8.5 and 91.8 m/s, respectively at 10.8 m/s inflow wind velocity (Bossanyi *et al.* 2011).

In this research, the 1/3 outer section of the CART II wind turbine blade (base case) along with two modified cases with different tip profiles, namely; tip O and tip R, are chosen for aerodynamic and aeroacoustic simulations. According to the wind tunnel experiment performed by Migliore (2009) on six different blade tip profiles, the outboard section of the rotor is the primary source of aeroacoustic emissions. The geometry of the blade sections that are used in this study is shown in Fig. 2.

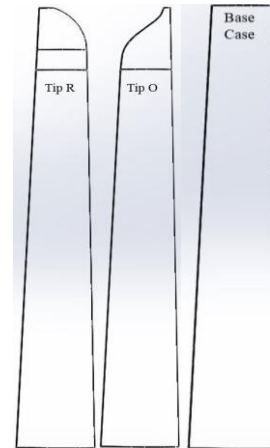


Fig. 2. Geometry of the base and the tip-equipped cases.

A 3D incompressible unsteady numerical simulation based on the finite volume solver, Ansys Fluent V17.2, was conducted to solve Navier-Stokes equations using the IDDES technique. The pressure-based solver, which is conventionally applied to solve low-Mach incompressible flow regimes, was used in this study. Due to the transient nature of the simulation, the PISO (Pressure Implicit with Splitting of Operator) algorithm, which ensures

stability and improves the convergence behavior of the numerical scheme, was chosen for velocity-pressure coupling. Spatial discretization has been done using the Green-Gauss node-based method for gradients. The second-order upwind scheme and the bounded central differencing scheme were chosen for solving pressure and momentum equations, respectively. Both turbulent kinetic energy and specific dissipation rate were discretized by a second-order upwind scheme. A bounded second-order implicit scheme was used for the transient algorithm.

The computational domain consists of a rotating and a stationary domain with a cylindrical interface in between. The relative motion of the two regions was taken into account using the sliding mesh technique.

The meshing process was conducted using the Pointwise V17.2. A hybrid meshing approach, using the structured grid on the blade surface and in the boundary layer, and tetrahedral elements elsewhere, was chosen for meshing the domain shown in Fig. 3. Due to the implementation of quad and prism elements inside the boundary layer, mesh quality statistics were quite satisfactory.

To resolve the whole boundary layer in which Navier-Stokes equations are solved directly, the height of the first row of elements surrounding the blade was set to be $5.10^{-6} m$ ensuring $y^+ < 1$ for all cells in the immediate vicinity of the blade. The computational domain and the boundary layer mesh are shown in Fig. 3. The number of elements for each simulated case is reported in Table 1.

Table 1. The size of the computational grid for each case

Cases	Base	Tip R	Tip O
No. of grid cells (10^6)	7.5	7.6	9.1

The simulations were performed on a single blade with periodic boundary conditions applied to account for the effect of the other. This helps simplify the

geometry and reduces the computational time due to fewer grid cells. The simulations were stable at a transient time step of $5.10^{-6} s$, owing to the small Courant number and accurate temporal discretization, and ran for a total simulated time of 0.3 s. The last 0.12 s, corresponding to the final 30° of rotation, were performed for acoustic calculations. The blade surface and rotary-stationary interfaces were chosen as acoustic sources to compute thickness-loading and total noise, respectively. The time-dependent surface pressure fluctuations were recorded as acoustic source data and were converted to the frequency domain using Fast Fourier Transform (FFT) for further investigation. The acoustic result of the base case, the outer section of CART II, was compared with the experimental data of Moriarty (Moriarty 2004) to validate the numerical simulation and a good agreement was observed.

Since the focus of this study is the tip vortex noise mechanism, and the tip vortex lower frequency range is approximately 1 kHz, corresponding to a period of 0.001 s, which is much smaller than the simulation period of 0.3 s, the duration simulated in this research is long enough to cover the process of tip vortex formation and its interaction with the blade trailing edge (Arakawa *et al.* 2005). Accordingly, the tip vortex and its associated acoustic features develop and are properly resolved in this simulation. However, longer run time, including several full rotations should be allowed, if low-frequency noise mechanisms such as; blade-tower interaction, blade passing frequency, separation, etc., or wake aerodynamics are of interest (Lee 2014; Ma *et al.* 2017; Zahle *et al.* 2009; Zahle and Sørensen, 2007). All the simulations were processed on a parallel 24 core, 2.4GHz clock frequency cluster. The required CPU time for each case was approximately 30 days.

5. RESULTS

5.1 Grid-Sensitivity and Aerodynamic Validation

Since FW-H acoustic analogy uses flow characteristics like pressure perturbations to

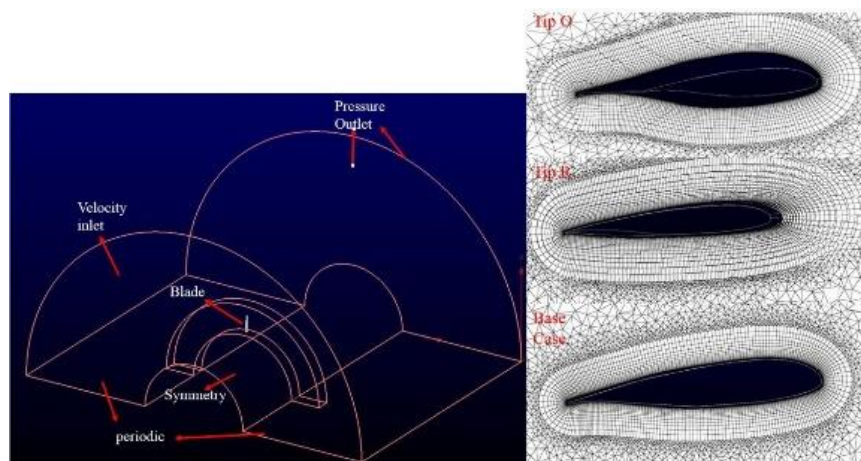


Fig. 3. Computational domain with the associated boundary conditions (Left), the boundary layer mesh for each case (right).

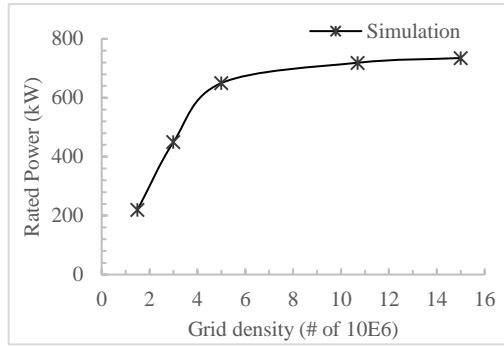


Fig. 4. Calculated CART II rated power (kW) at different grid densities.

calculate the SPL at a receiver's location, it is necessary to accurately resolve the aerodynamic field around the blades, especially near the tip region. To identify suitable chord-wise and spanwise mesh spacing values, preliminary simulations with five different grid densities were conducted using a single CART II blade (Fig. 7) at the wind velocity of 12.5 m/s, corresponding to the rated power of 660 kW. As shown in Fig. 4, the calculated rated power nearly flats out beyond a grid size of roughly 11 million elements. Hence, the grid ratios found during the preliminary study were adopted to the geometries in Fig. 2, which results in the total grid sizes reported in Table 1. However, more points had to be clustered in the vicinity of the O-type tip region to better resolve the profile curvature near its trailing edge, which leads to yet a higher mesh size than the other two.

For the sake of further validation, the average aerodynamic power at different wind velocities was calculated and compared with the corresponding experimental values of the CART II power curve (Griffin 2000). Overall, the graphs in Fig. 5 show good agreement between the simulated and experimental output. The average error is around 10% percent which is considered satisfactory for the present study. Note that the power overestimation of the numerical method in all points is mainly due to the omittance of losses from the tower effect, mechanical coupling, electrical components, and other losses that are accounted for in the experimental data.

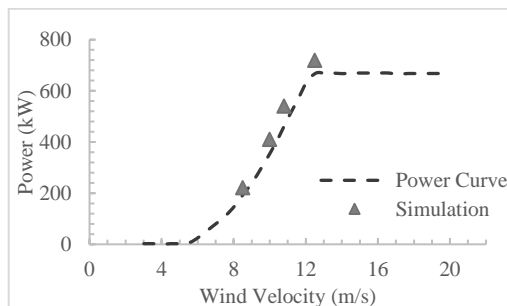


Fig. 5. Comparison of the calculated power output with the experimental data (Griffin 2000).

5.2 Aeroacoustic Validation

Before any discussion on the aeroacoustic results, it is of paramount importance to validate FW-H acoustic analogy output for the present study.

As stated in Sec. 5.1, only one blade of the whole CART II Wind Turbine is simulated. With the assumption of the same acoustic characteristics for the other blade, the total SPL of the wind turbine is calculated as follows:

$$L_{2blades} = 10 \log_{10} \left(\left(\frac{\hat{p}_{one\ blade}^2}{\hat{p}_{ref}^2} \right) + \left(\frac{\hat{p}_{one\ blade}^2}{\hat{p}_{ref}^2} \right) \right) = 10 \log_{10} \left(2 \times \left(\frac{\hat{p}_{one\ blade}^2}{\hat{p}_{ref}^2} \right) \right) = 3.01 + L_{one\ blade} \quad (12)$$

The SPL is a logarithmic measure of the effective sound pressure with respect to a reference value of $\hat{p}_{ref} = 2 * 10^{-5} \text{ pa}$, and is defined as follows (Wagner *et al.* 1996):

$$L_p = 10 * \log \left(\frac{\hat{p}^2}{\hat{p}_{ref}^2} \right) \quad (13)$$

The acoustic emission of CART II wind turbine was investigated by Moriarty *et al.* (Moriarty 2004). Figure 6 shows the acoustic results for the CART II wind turbine model compared with the experimental data from Moriarty. The effect of the second blade was added to the simulated SPL diagram.

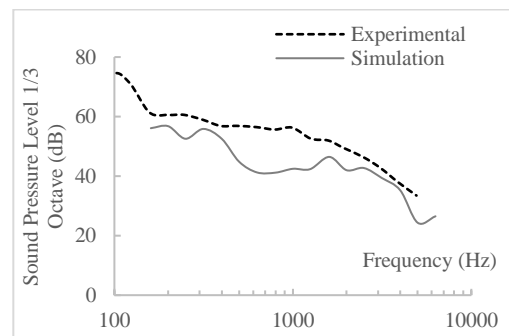


Fig. 6. Comparison of the simulated CAA results for CART II with the acoustic field measurements.

According to the graph, the experimental values in the whole frequency range are higher than those calculated by the FW-H acoustic analogy. The difference between the two curves is attributed to two factors. First, the model's inability to consider the mechanical and background noise, embedded in the measured data. Second, omission of the inner blade section and hub flow separation noise, visible in Fig. 7, and the blade-tower interaction noise and their associative effects on the SPL due to modeling only the outboard section of the CART II blade. The latter is in agreement with the results of the Ma *et al.* study (Ma *et al.* 2017), in which investigation of the whole rotor with/without the tower presence showed significant discrepancies in the SPL graphs of two

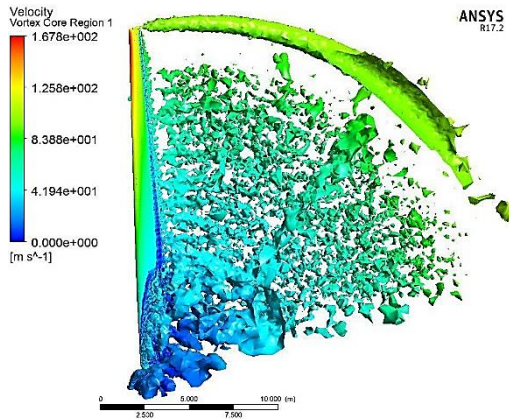


Fig. 7. The Iso-surface of turbulent vortical structures in the wake for $Q=20 \text{ s}^{-2}$ colored by the velocity magnitude.

cases at the 300 Hz to 1500 Hz frequency range. The authors concluded that the difference originates from the blade-tower interaction noise mechanism.

Figure 7 is rendered based on Q-criterion, which is the second invariant of the velocity gradient tensor and is defined as, (Chakraborty *et al.* 2005);

$$Q = \frac{1}{2} [\Omega_{ij}\Omega_{ij} - S_{ij}S_{ij}] \quad (14)$$

$$S_{ij} = \frac{1}{2} \left(\frac{\partial u_i}{\partial x_j} + \frac{\partial u_j}{\partial x_i} \right), \Omega_{ij} = \frac{1}{2} \left(\frac{\partial u_i}{\partial x_j} - \frac{\partial u_j}{\partial x_i} \right) \quad (15)$$

5.3 Aeroacoustic result and the SPL data of the base case (outboard section of CARTII)

The total and the sum of thickness and loading noise spectrum, hereafter thickness-loading noise, for the outboard section of CART II is shown in Fig. 8. As stated before, aerodynamic noise generated by the wind turbine is comprised of the thickness, loading, and quadrupole noise sources. The thickness-loading noise and the total noise are calculated by integrating

sources over the blade surface and the interface surface, respectively. The difference between the total and thickness-loading noise determines the contribution of quadrupole sources.

Noted that the tip speed ratio at the rated power for CART II is 8.5, which is relatively high. Therefore, it can be assumed that the flow at the outboard section of the blade is primarily tangential (Zahle *et al.* 2009). Accordingly, any differences in the graphs of total and thickness-loading sound pressure levels are due to the tip vortex formation and its associated acoustic sources. In other words, the tip vortex shedding and its interactions with the blade trailing edge are the primary reasons for the discrepancies between the two noise spectra. Figure 9 shows the flow field turbulent vortical structures around and in the immediate vicinity of the tip region. At first sight, the assumption of tangential flow at the outer section of the blade is verified. Furthermore, the tip vortex formation at the very end of the blade and its interaction with the blade trailing edge is clearly visible. Therefore, Fig. 9 visually demonstrates the reasons for differences in the graphs of Fig. 8.

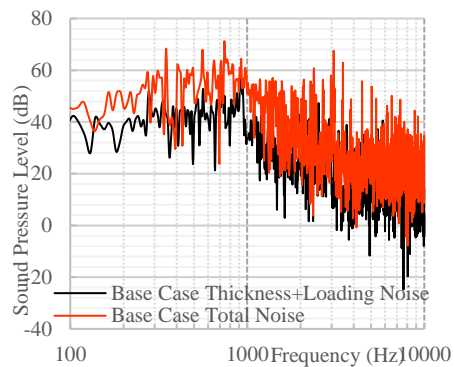


Fig. 8. The SPL of thickness-loading and total noise of the CART II blade's outboard section (base case).

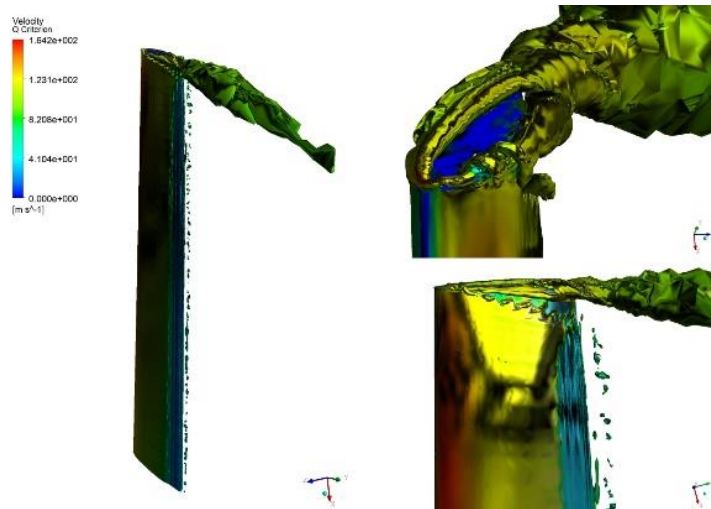


Fig. 9. The Iso-surface of turbulent vortical structures near the tip region of the base case for $Q=3000 \text{ s}^{-2}$ colored by the velocity magnitude.

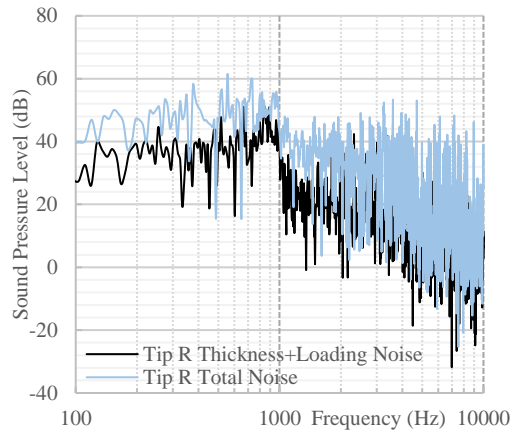


Fig. 10. The SPL of thickness-loading and total noise of the tip R case.

5.4 Aeroacoustic results and the SPL data of tip O and tip R configurations

In the following, SPL graphs of two modified cases, i.e., tip R and tip O, are discussed, and their total SPL graph is compared. Then, the turbulent vortical structures near the tip region of the two cases are illustrated to help understand discrepancies in the total SPL graph.

Figures 10 and 11 depict the SPL of total and thickness-loading noise for tip R and tip O, respectively. Similar to the trend in Fig. 8, the total SPL is higher than the thickness-loading SPL at mid to high frequencies ranging from 1 kHz to 5 kHz, which is attributed to the tip vortex shedding and its interaction with the trailing edge. Additionally, further investigation of the graphs in Figs.10 and 11 reveals that the difference between the total and the thickness-loading SPL for tip O is smaller than that of tip R. This is due to the reduced tip vortex intensity and, subsequently, the minor contribution of quadrupole sources in the total noise of the former.

5.4.1 The relationship between the total SPL graph and coherent vortical structures at the tip region

The total SPL graph for tip R and tip O is illustrated in Fig. 12 and it is clear that tip R has a higher level of sound pressure at the entire frequency range than tip O. As mentioned previously, one of the quadrupole broadband noise sources is the formation of high-velocity gradients and highly unsteady turbulent structures near the tip of wind turbine blade (Wagner *et al.* 1996). Based on Powell's equation, formation and motion of eddies in turbulent flows (Reynolds stresses) are the primary sources of sound generation, neglecting the effects of heat release, entropy, and viscous stress terms in Lighthill's acoustic tensor (Powell 1964).

$$\frac{1}{c_0^2} \frac{\partial^2 p'}{\partial t^2} - \nabla^2 p' = \nabla \cdot (\rho \vec{\omega} \times \vec{u}) \quad (16)$$

The $\nabla \cdot (\rho \vec{\omega} \times \vec{u})$ term determines the contributions from the flow vortical motions to the sound generation. c_0, ω, u are attributed to the sound

velocity, vortex, and medium velocity, respectively. Considering Powell's theory and Figs. 13–15, the higher SPL of total noise in the tip R case can be explained.

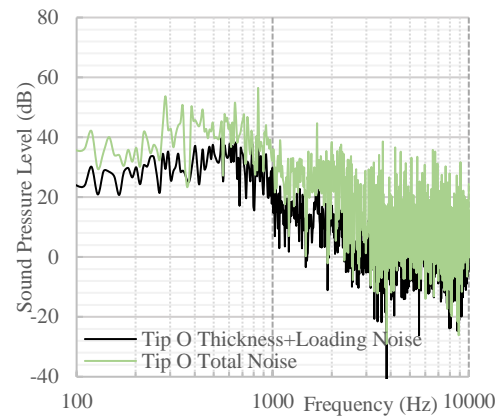


Fig. 11. The SPL of thickness-loading and total noise of the tip O case.

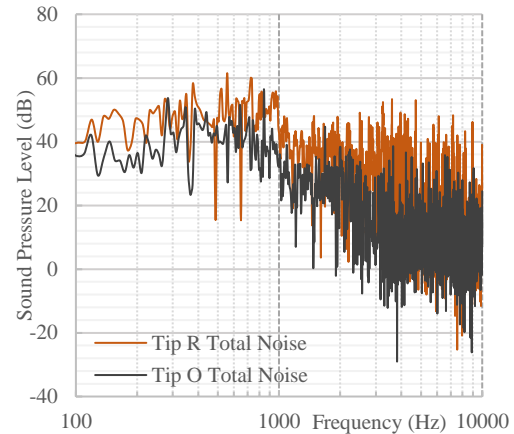


Fig. 12. Comparison of the total noise SPL diagrams of the tip O and the tip R cases.

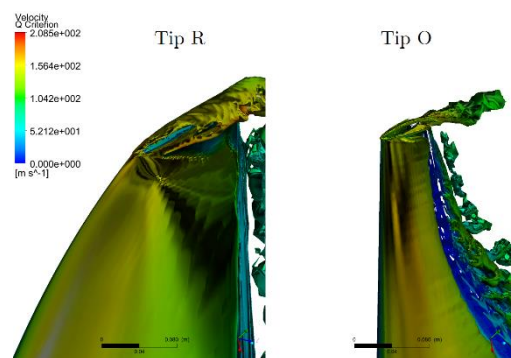


Fig. 13. Formation of tip vortices for tip R (left) and tip O (right) (the same scale is applied to both figures.)

Figure 13 shows turbulent vortical structures in the vicinity of the tip region for the tip R and the tip O cases. Since both pictures have the same scale, it can

be observed that the vortices shed from the tip O case are significantly smaller than those shed from the tip R case. Reduced tip vortex structures in the tip O design are a reason for lower total SPL at mid to high-frequencies range than the tip R.

Figures 12 and 13 show the instantaneous vortical structures around the tip region of both cases. Through further investigation of these figures, another reason for the lower total sound pressure levels of tip O compared to tip R is detected. As shown in the magnified region of Fig. 14, the flow is detached before reaching the trailing edge of tip O, leading to developing a small separation region at the suction side of the blade. In contrast, the flow is fully attached to the blade surface, and vortices are discarded from the trailing edge of the tip R case. It is worth mentioning that instabilities and turbulent eddies developed in the boundary layer, especially aft of the suction side's trailing edge, and due to the flow acceleration, are quadrupole sound sources, emitting intense high-frequency noise (Wagner *et al.* 1996). Separation of the flow before it reaches the trailing edge in the tip O case causes the turbulent flow detachment from the blade surface at the tip region, thus preventing the generation and radiation

of intense high-frequency “Turbulent-Boundary-Layer Trailing Edge Noise”. Although flow separation itself is another source of sound generation, it is not dominant at the mid to high frequencies. Therefore, it is the second reason for the higher SPL of total noise in the tip R case.

5.4.2 Far-field noise prediction of tip O and R designs

Using FW-H acoustic analogy, the OASPL perceived by a receiver located downwind of the rotor at the ground level and at a distance of $H + D/2 = 58$ m according to the IEC61400-11 standard, where H and D, are the hub height and the rotor diameters, respectively, is computed for all three cases and presented in Table 2 along with their respective torque values in N.m. Given the Total noise values, it can be concluded that tip O and tip R modified cases emit 5.0 % and 2.0% less noise than the base design, respectively. Additionally, the difference between the Total and the T+L noises steadily decreases from 4.0 % in the base design to 3.3% in tip R and 2.4% in tip O, which confirms the results in section 5 regarding the reduced quadrupole sources intensities, i.e., tip vortices.

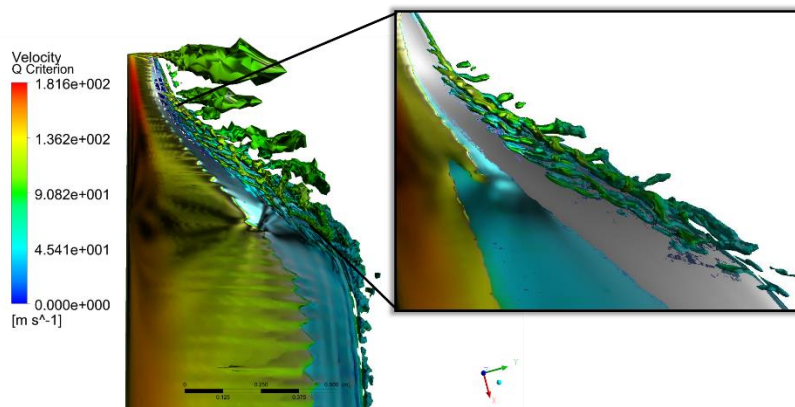


Fig. 14. The iso-surface of turbulent vortical structures near the tip region of the tip O case for $Q=3000$ s^2 colored by the velocity magnitude.

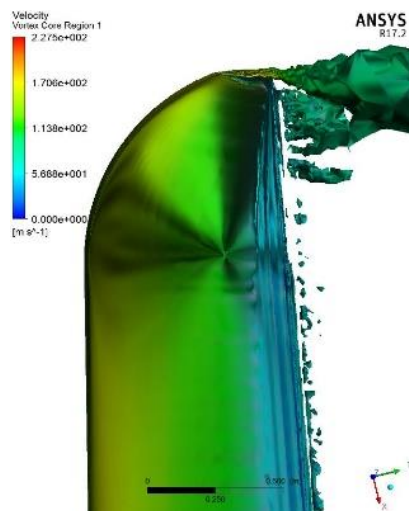


Fig. 15. The iso-surface of turbulent vortical structures near the tip region of the tip R case for $Q=3000$ s^2 colored by the velocity magnitude.

Table 2. The OASPL measured 58 m downwind the rotor and the torque value for the modeled cases (values inside parenthesis indicate changes from the base case)

	Total Noise (dB)	T+L Noise (dB)	Torque (N.m)
Base	71.29	68.44	27750
Tip O	67.75 (- 5.0 %)	66.15 (- 3.3 %)	27136 (- 2.2 %)
Tip R	69.84 (- 2.0 %)	67.55 (- 1.3 %)	27515 (- 0.8 %)

Finally, while tip O and tip R produce 2.2 % and 0.8 % less torque than the base case, their noise level is 3.5 dB and 1.4 dB lower, respectively. It indicates the suitability of the proposed design for improving the CART II aeroacoustics behavior without significantly affecting its aerodynamic performance.

6. CONCLUSION

In this research, the aerodynamic and aeroacoustic characteristics of the flow field around the outboard section of the CART II wind turbine blade and two modified tip profiles, namely; tip O and tip R were studied. The IDDES technique was used to resolve the instantaneous turbulent flow field around the tip region of the proposed designs, while the Ffowcs William and Hawkins (FW-H) acoustic analogy was employed to predict the far-field noise.

Simulations were conducted at the same flow conditions as Moriarty’s experiment. The one-third octave SPL graph obtained from this study was compared to the one presented by Moriarty, and good agreement was observed.

Omittance of noise from the mechanical equipment and blade-tower interaction is the primary reason for the difference between the simulated and measured SPL graph of the CART II wind turbine blade. The latter is in confirmation with the Ma *et al.* study (Ma *et al.* 2017).

Considering the total and thickness-loading SPL graphs and the contours of turbulent vortical structures in the tip region of the base case, the difference between the two graphs is due to the tip vortex and its interaction with the trailing edge noise mechanisms, which are essentially quadrupole sound sources.

Investigating the total and thickness-loading noise spectrum of the tip O and the tip R cases separately revealed the same trend observed in the base case. Moreover, the difference between the total SPL and thickness-loading SPL for the tip O was lower than the tip R, which was identified to be due to the diminished tip vortices intensity, leading to the reduction of the tip vortex noise emission.

Comparing the total SPL graphs in conjunction with contours of turbulent vortical structures for tip O and tip R helped detect two main reasons for the lower total SPL of the former. First, reduction in size and intensity of the tip vortices and its subsequent

interaction with the trailing edge. Second, early flow separation before reaching the trailing edge of the tip O hindering the process of generation and radiation of intense high-frequency “Turbulent-Boundary-layer Trailing-Edge Noise mechanism”.

Finally, the OASPL and torque for all cases were compared and it was shown that despite limited torque reduction in the modified cases, their aeroacoustic characteristics notably improved compared to the base design.

REFERENCES

- Arakawa, C., O. Fleig, M. Iida and M. Shimooka (2005). *Numerical Approach for Noise Reduction of Wind Turbine Blade Tip with Earth Simulator*. 2(March), 11–33.
- Bossanyi, E. A., A. D. Wright and P. A. Fleming (2011). Controller field tests on the NREL CART3 turbine. UPWIND REPORT: 11593/BR/09. *Work, December*.
- Brentner, K. S. (1987). Prediction of helicopter rotor discrete frequency noise for three scale models. *Journal of Aircraft* 25(5), 420–427.
- Cai, X., R. Gu, P. Pan and J. Zhu (2016). Unsteady aerodynamics simulation of a full-scale horizontal axis wind turbine using CFD methodology. *Energy Conversion and Management* 112, 146–156.
- Chakraborty, P., S. Balachandar and R. J. Adrian (2005). On the relationships between local vortex identification schemes. *Journal of Fluid Mechanics* 535, 189–214.
- Cho, T., C. Kim and D. Lee (2010). Acoustic measurement for 12% scaled model of NREL Phase VI wind turbine by using beamforming. *Current Applied Physics* 10(2), S320–S325.
- Dai, K., A. Bergot, C. Liang, W.-N. Xiang and Z. Huang (2015). Environmental issues associated with wind energy – A review. *Renewable Energy* 75, 911–921.
- Delbari, S. H., A. Nejat, M. H. Ahmadi, A. Khaleghi and M. Goodarzi (2019). Numerical modeling of aeroacoustic characteristics of different savonius blade profiles. *International Journal of Numerical Methods for Heat & Fluid Flow* 30(6), 3349-3369.
- Ebrahimi, A. and R. Mardani (2018). Tip-Vortex Noise Reduction of a Wind Turbine Using a Winglet. *Journal of Energy Engineering* 144(1), 04017076.
- Ewert, R. and W. Schröder (2004). On the simulation of trailing edge noise with a hybrid LES/APE method. *Journal of Sound and Vibration* 270(3), 509–524.
- Ghasemian, M. and A. Nejat (2015a). Aero-acoustics prediction of a vertical axis wind turbine using Large Eddy Simulation and acoustic analogy. *Energy* 88, 711–717.

- Ghasemian, M. and A. Nejat (2015b). Aerodynamic noise prediction of a Horizontal Axis Wind Turbine using Improved Delayed Detached Eddy Simulation and acoustic analogy. *Energy Conversion and Management* 99, 210–220.
- Göçmen, T. and B. Özerdem (2012). Airfoil optimization for noise emission problem and aerodynamic performance criterion on small scale wind turbines. *Energy* 46(1), 62–71.
- Griffin, D. A. (2000). *Turbine (ART) Aerodynamic Design of ART-2B Rotor Blades NREL Advanced Research Turbine (ART) Aerodynamic Design of ART-2B Rotor Blades*. August.
- Jianu, O., M. A. Rosen and G. Naterer (2012). Noise Pollution Prevention in Wind Turbines: Status and Recent Advances. *Sustainability* 4, 1104–1117.
- Kaviani, H. R. and A. Nejat (2017). Aerodynamic noise prediction of a MW-class HAWT using shear wind profile. *Journal of Wind Engineering and Industrial Aerodynamics* 168, 164–176.
- Lee, S. (2014). Numerical and experimental study of aerodynamic noise by a small wind turbine. *Renewable Energy* 65, 108–112.
- Ma, P., F.-S. Lien and E. Yee (2017). Coarse-resolution numerical prediction of small wind turbine noise with validation against field measurements. *Renewable Energy* 102, 502–515.
- Maizi, M., M. H. Mohamed, R. Dizene and M. C. Mihoubi (2018). Noise reduction of a horizontal wind turbine using different blade shapes. *Renewable Energy* 117, 242–256.
- Menter, F. R. (1994). Two-equation eddy-viscosity turbulence models for engineering applications. *AIAA Journal* 32(8), 1598–1605.
- Migliore, P. (2009). *The Potential for Reducing Blade-Tip Acoustic Emissions For Small Wind Turbines The Potential for Reducing Blade-Tip Acoustic Emissions For Small Wind Turbines* (Issue February).
- Mo, J. O. and Y. H. Lee (2011). Numerical simulation for prediction of aerodynamic noise characteristics on a HAWT of NREL phase VI. *Journal of Mechanical Science and Technology* 25(5), 1341–1349.
- Mohamed, M. H. (2014). Aero-acoustics noise evaluation of H-rotor Darrieus wind turbines. *Energy* 65, 596–604.
- Mohamed, M. H. (2016). Reduction of the generated aero-acoustics noise of a vertical axis wind turbine using CFD (Computational Fluid Dynamics) techniques. *Energy* 96, 531–544.
- Moriarty, P. J. (2004). Development and Validation of a Semi-empirical Wind Turbine Aeroacoustic Code. *AIAA Conference* 53(9), 266–276.
- Mostafaiepour, A. (2013). Economic evaluation of small wind turbine utilization in Kerman, Iran. *Energy Conversion and Management* 73, 214–225.
- Oerlemans, S. (2009). *Detection of aeroacoustic sound sources on aircraft and wind turbines*.
- Powell, A. (1964). Theory of Vortex Sound. *The Journal of the Acoustical Society of America* 36(1), 177–195.
- Shur, M. L., P. R. Spalart, M. K. Strelets and A. K. Travin (2008). A hybrid RANS-LES approach with delayed-DES and wall-modelled LES capabilities. *International Journal of Heat and Fluid Flow* 29(6), 1638–1649.
- Solís-Gallego, I., A. Meana-Fernández, J. M. Fernández Oro, K. M. Argüelles Díaz and S. Velarde-Suárez (2018). LES-based numerical prediction of the trailing edge noise in a small wind turbine airfoil at different angles of attack. *Renewable Energy* 120, 241–254.
- Stol, K. A. (2004). Geometry and structural properties for the controls advanced research turbine (CART) from model tuning. *Nrel/Sr, September*, 500–32087. <http://www.nrel.gov/docs/fy04osti/32087.pdf>
- Tadamasa, A. and M. Zangeneh (2011). Numerical prediction of wind turbine noise. *Renewable Energy* 36(7), 1902–1912.
- Wagner, S., R. Bareiß and G. Guidati (1996). *Wind Turbine Noise*. Springer Berlin Heidelberg.
- Wasala, S. H., R. C. Storey, S. E. Norris and J. E. Cater (2015). Aeroacoustic noise prediction for wind turbines using Large Eddy Simulation. *Journal of Wind Engineering and Industrial Aerodynamics* 145, 17–29.
- Williams, J. E. F. and D. L. Hawkings (1969). Sound Generation by Turbulence and Surfaces in Arbitrary Motion. *Philosophical Transactions of the Royal Society of London A: Mathematical, Physical and Engineering Sciences*, 264(1151). <http://rsta.royalsocietypublishing.org/content/264/1151/321>
- Xiao, L., Z. Xiao, Z. Duan and S. Fu (2015). Improved-Delayed-Detached-Eddy Simulation of cavity-induced transition in hypersonic boundary layer. *International Journal of Heat and Fluid Flow* 51, 138–150.
- Zahle, F. and N. N. Sørensen (2007). On the influence of far-wake resolution on wind turbine flow simulations. *Journal of Physics: Conference Series* 75(1).
- Zahle, F., N. N. Sørensen and J. Johansen (2009). Wind turbine rotor-tower interaction using an incompressible overset grid method. *Wind Energy* 12(6), 594–619.